Quantum algorithms for grid-based variational time evolution

Pauline J. Ollitrault,[1] Sven Jandura,[1,*] Alexander Miessen,[1] Irene Burghardt,[2]
Rocco Martinazzo,[3,4] Francesco Tacchino,[1] and Ivano Tavernelli[1,†]

[1] *IBM Quantum, IBM Research – Zurich, Säumerstrasse 4, 8803 Rüschlikon, Switzerland*
[2] *Institute of Physical and Theoretical Chemistry, Goethe University Frankfurt, Max-von-Laue-Str. 7, D-60438 Frankfurt/Main, Germany*
[3] *Department of Chemistry, Università degli Studi di Milano, Via Golgi 19, 20133 Milano, Italy*
[4] *Istituto di Scienze e Tecnologie Molecolari, CNR, via Golgi 19, 20133 Milano, Italy*

(Dated: March 8, 2022)

The simulation of quantum dynamics calls for quantum algorithms working in first quantized grid encodings. Here, we propose a variational quantum algorithm for performing quantum dynamics in first quantization. In addition to the usual reduction in circuit depth conferred by variational approaches, this algorithm also enjoys several advantages compared to previously proposed ones. For instance, variational approaches suffer from the need for a large number of measurements. However, the grid encoding of first quantized Hamiltonians only requires measuring in position and momentum bases, irrespective of the system size. Their combination with variational approaches is therefore particularly attractive. Moreover, heuristic variational forms can be employed to overcome the limitation of the hard decomposition of Trotterized first quantized Hamiltonians into quantum gates. We apply this quantum algorithm to the dynamics of several systems in one and two dimensions. Our simulations exhibit the previously observed numerical instabilities of variational time propagation approaches. We show how they can be significantly attenuated through subspace diagonalization at a cost of an additional $\mathcal{O}(MN^2)$ 2-qubit gates where M is the number of dimensions and N^M is the total number of grid points.

I. INTRODUCTION

Quantum mechanics is at the heart of most chemical processes, whose description is generally based on electronic structure calculations combined with reaction rate theories (typically for slow ground-state processes), or else nuclear wavepacket dynamics (typically for ultrafast photo-induced processes). Quantum tunneling can enhance chemical reaction rates [1, 2], and quantum effects are manifest in all types of molecular spectroscopies [3]. As a more specific example, recent advances in photochemistry have shown that the combination of various spin excitons can increase the efficiency of photochemical reactions [4]. As the fundamental understanding of these chemical processes became necessary, femtosecond [5, 6] and attosecond [7–9] time-resolved pump-probe lasers were developed to follow, in real time, the motion of the nuclei and electrons, respectively. Along with these experimental discoveries, advances in theoretical approaches leaned towards the study of molecular processes in a fully quantum mechanical way.

As a first step, this led to the development of integration methods to solve the time-dependent Schrödinger equation (TDSE) [10–14]. However, even on modern supercomputers, this task is limited to molecules composed of only a few atoms as the required computational resources scale exponentially with the number of degrees of freedom [1, 15, 16]. To reduce the computational cost, a compact basis representation of the system is required. A natural way of doing so is to work with a time-dependent basis, which follows the evolution of the system. This strategy has been applied to the solution of the TDSE through the variational principle in the time-dependent Hartree (TDH) [17, 18] and the more general multi-configuration time-dependent Hartree (MCTDH) approaches [19, 20]. In its exact formulation, MCTDH maintains an exponential scaling in the number of basis functions. Further approximations were introduced to reduce the basis set size and lower its computational costs. These approximations led to the Gaussian MCTDH (G-MCTDH) [21], the multilayer MCTDH (ML-MCTDH) [22–25] and an analogous Gaussian-based ML-GMCTDH variant [26], the MCTDHn [27] and its multi-reference extension (MR-MCTDHn) [15], the variational multiconfigurational Gaussian (vMCG) [28, 29], as well as the coupled coherent states (CCS) approximation [30–32] and Multiple-Spawning [33, 34]. Despite this impressive theoretical progress, accurate applications of the foregoing algorithms remain restricted to molecules with less than a few tens of collective degrees of freedom [1, 15, 34, 35].

An alternative path towards the efficient modeling of quantum dynamics is to switch towards a new computational paradigm. In particular, quantum computers have the potential to simulate quantum systems in polynomial time and memory [36, 37]. Following Feynman's thesis, Wiesner [38] and Zalka [39] first designed a framework to simulate molecular quantum dynamics on a digital quantum computer with a grid encoding of real space. This framework was then made concrete and applied to the simulation of several small nuclear quantum systems

* present address: ISIS (UMR 7006), University of Strasbourg, 67000 Strasbourg, France
† ita@zurich.ibm.com

in rectangular or harmonic potentials [40–44]. More recently, it was also extended to the simulation of the non-adiabatic dynamics of nuclear wavepackets [45, 46]. All these approaches share the same circuit representation of the time evolution operator, obtained from Trotter approximation of the latter [47]. However, in general, this leads to very deep quantum circuits, which greatly exceed the capacities of present quantum hardware due to their limited coherence times. This is particularly true when the Hamiltonian is given in first quantization as, in this case, an efficient encoding of even a single Trotter step into a quantum circuit is cumbersome [45, 48, 49]. As a consequence, the type of implementable potentials is restricted. For instance, all the works cited above only present dynamics under potentials that can be defined with a polynomial function of the position. It is worth emphasising here that active research is undergoing to implement Coulombic potentials. [49–52]

To address the issue of circuit depth, variational time evolution (VTE) quantum algorithms were proposed. For a comprehensive overview see for instance Refs. 53, 54. Relying on an iterative exchange of information between a classical and a quantum computer, these algorithms allow to work with shallower quantum circuits of constant depth in time. In particular, Li and Benjamin [55] first showed how to use a variational principle to simulate the real time dynamics of quantum systems and applied it to a quantum Ising model.

The goal of the present work is to extend this approach to the simulation of wavepacket quantum dynamics in a grid-based encoding for general Hamiltonians given in first quantization. We first recall the theory of variational quantum time evolution and highlight the differences between the first and second quantization formalisms of quantum mechanics within this context. We then discuss the wavefunction representation and the potential of this approach for a quantum advantage. We apply the quantum algorithm in a quantum emulator for the simulation of the dynamics of different systems in one dimension, namely a free particle, a particle in a harmonic potential, and a particle interacting with an Eckart barrier. As a next step, we apply the algorithm to the evolution of a wavepacket in a two-dimensional "Mexican hat" potential. Finally, we conclude and give an outlook on future developments and applications.

II. THEORY

A. The time-dependent variational principle

The variational approach to quantum dynamics aims to approximate the solution of the TDSE on a low-dimensional submanifold of the full Hilbert space. The trial wavefunction defined on this manifold $|\psi(\boldsymbol{\theta}(t))\rangle$ is parameterized by a set of n_p time-dependent parameters, $\boldsymbol{\theta}(t) = \{\theta_1(t), ..., \theta_{n_p}(t)\}$. A time-dependent variational principle (TDVP) defines the optimal evolution of the parameters within the submanifold of the full Hilbert space. There exist different formulations of the TDVP. For Kähler manifolds, i. e., when the tangent space is a complex subspace [56], all the different formulations lead to the same equations of motion for the variational parameters. However, this is not the case for unitary parameterizations of the type

$$|\psi(\boldsymbol{\theta}(t))\rangle = \mathcal{U}(\boldsymbol{\theta}(t))\,|\phi\rangle\,, \tag{1}$$

where $|\phi\rangle$ is a reference state and $\mathcal{U}(\boldsymbol{\theta}(t))$ is a unitary operator (e.g., the quantum circuit) depending on real parameters $\boldsymbol{\theta}(t)$ [56]. In this case, the equations of motion differ and hold distinct properties such as the conservation of the norm or the energy. Recent works [53, 56–59] promoted the use of the equations of motion derived from the McLachlan variational principle due to of their higher numerical stability [56]. For a given Hamiltonian $\mathcal{H}$, these equations, when accounting for a global phase mismatch (see Ref. 53), read

$$\mathrm{M}\dot{\boldsymbol{\theta}} = \mathrm{V}\ , \tag{2}$$

with

$$M_{kj} = \Re\Big(\langle\partial_{\theta_k}\psi|\partial_{\theta_j}\psi\rangle - \langle\partial_{\theta_k}\psi|\psi\rangle\,\langle\psi|\partial_{\theta_j}\psi\rangle\Big)\ , \tag{3}$$

and

$$V_k = \Im\Big(\langle\partial_{\theta_k}\psi|\,\mathcal{H}\,|\psi\rangle - \langle\partial_{\theta_k}\psi|\psi\rangle\,\langle\psi|\,\mathcal{H}\,|\psi\rangle\Big)\ . \tag{4}$$

For a regular parametrization, Eq. (3) represents a quantum metric (the Fubini-Study metric) in parameter space. In conjuction with Eq. (3), Eq. (4) shows that Eq. (2) results from the orthogonal projection of the exact time-derivative of $|\psi\rangle$ on the variational manifold. These equations of motion are used throughout this work.

B. 1st vs 2nd quantization

The calculation of the M_{kj} and V_k matrix and vector elements are classically hampered by the high dimension of $|\psi(\boldsymbol{\theta})\rangle$. Instead, they can be efficiently measured on a trial wavefunction encoded in the state of a qubit register. In this case, the trial wavefunction $|\psi(\boldsymbol{\theta})\rangle$ (see Eq. (1)) is defined by the variational parameters $\boldsymbol{\theta}$, which enter the quantum circuit $\mathcal{U}$ as rotation angles of the type $R_X(\theta_k) = e^{-i\theta_k X/2}$, $R_Y(\theta_k) = e^{-i\theta_k Y/2}$, or $R_Z(\theta_k) = e^{-i\theta_k Z/2}$. Here, X, Y, and Z are the Pauli matrices. The measurement of analytic gradients on quantum computers was discussed in Ref. 60. Here, we detail the technical differences between the algorithm for Hamiltonians defined as a sum of Pauli operators and for first quantized Hamiltonians encoded on a grid.

Consider the following general form for a variational quantum circuit $\mathcal{U}(\boldsymbol{\theta}(t)) \equiv \mathcal{U}(\boldsymbol{\theta})$ comprising n_p parame-

ters and acting on N_q qubits

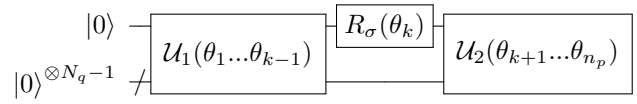

with $\sigma \in \{X, Y, Z\}$. Then, $\partial_{\theta_k}\mathcal{U}(\boldsymbol{\theta})$ can be computed from the following quantum circuit

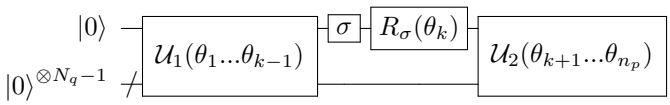

All matrix elements of M and V can therefore be written as $\langle\phi|\,\mathcal{W}_1^\dagger\mathcal{O}\mathcal{W}_2\,|\phi\rangle$, where $\mathcal{W}_1 \equiv \mathcal{W}_1(\boldsymbol{\theta})$ and $\mathcal{W}_2 \equiv \mathcal{W}_2(\boldsymbol{\theta})$ are unitary quantum circuits, and $\mathcal{O}$ is a general operator.

We start by considering the system Hamiltonian in second quantization. After mapping the second quantized operators to Pauli operators [61, 62], the Hamiltonian is written as a weighted sum of Pauli tensor strings, $\mathcal{H} = \sum_p c_p\mathcal{P}_p$. With $\mathcal{O} = \mathcal{H}$, the general form of the expectation value given above becomes

$$\langle\phi|\,\mathcal{W}_1^\dagger \sum_p c_p\mathcal{P}_p\mathcal{W}_2\,|\phi\rangle = \sum_p c_p\,\langle\phi|\,\mathcal{W}_1^\dagger\mathcal{W}_{2,p}\,|\phi\rangle \ , \quad (5)$$

where $\mathcal{W}_{2,p} = \mathcal{P}_p\mathcal{W}_2$. Each term can then be efficiently measured as [63]

$\langle\phi|\,\mathcal{W}_1^\dagger\mathcal{W}_{2,p}\,|\phi\rangle \equiv$

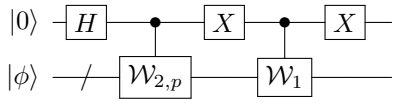

(6)

In the Supplemental Material, we detail the steps of the above quantum circuit, verifying Eq. (6).

In this work, however, we will focus on Hamiltonians expressed in first quantization,

$$\mathcal{H} = \frac{\boldsymbol{p}^2}{2m} + \mathcal{V}(\boldsymbol{r}) \ , \quad (7)$$

where $\boldsymbol{p}$ is the momentum, m the mass, and $\mathcal{V}(\boldsymbol{r})$ the potential given as a function of the position $\boldsymbol{r}$. $\mathcal{H}$ describes an M-dimensional systems. The time-evolution is directly performed in momentum and position space, discretized on a grid. The N points, per dimension, of the grid are encoded in the basis states of $N_q = \log_2(N)$ qubits. The total number of qubits is then MN_q. In this case, no explicit transformation to a basis representation is required, saving the numerical effort associated with such computations, which would scale as the square of the basis set size [64].

The expectation value of the Hamiltonian is now simply obtained from two sets of measurements, one in the momentum basis and one in the position basis. This gives a clear advantage in the calculation of the right-hand side of Eq. 2, which requires measuring $\langle\psi(\boldsymbol{\theta})|\,\mathcal{H}\,|\psi(\boldsymbol{\theta})\rangle$ and $\Im(\langle\partial_{\theta_k}\psi(\boldsymbol{\theta})|\,\mathcal{H}\,|\psi(\boldsymbol{\theta})\rangle)$. The first one is straightforward and reduces to measuring the expectation values $\langle\psi(\boldsymbol{\theta})|\,\boldsymbol{p}^2\,|\psi(\boldsymbol{\theta})\rangle$ and $\langle\psi(\boldsymbol{\theta})|\,\mathcal{V}(\boldsymbol{r})\,|\psi(\boldsymbol{\theta})\rangle$. In practice, this is obtained by repeatedly preparing and measuring the state $|\psi(\boldsymbol{\theta})\rangle$ in the computational (position) basis. For each outcome of the binary representation of $\boldsymbol{r}$, $\mathcal{V}(\boldsymbol{r})$ is classically computed and $\langle\psi(\boldsymbol{\theta})|\,\mathcal{V}(\boldsymbol{r})\,|\psi(\boldsymbol{\theta})\rangle$ is obtained by averaging over all realizations of $\mathcal{V}(\boldsymbol{r})$. The same is done for the kinetic term by measuring in the momentum basis, i. e., applying a quantum Fourier transform (QFT) right before the measurement (see Ref. [45]).

Let's now consider the calculation of the components V_k,

$$\Im\big(\,\langle\partial_{\theta_k}\psi(\boldsymbol{\theta})|\mathcal{H}\,|\psi(\boldsymbol{\theta})\rangle\,\big) = \frac{1}{2}\Re\big(\,\langle\phi|\,\mathcal{W}(\boldsymbol{\theta})^\dagger\mathcal{H}\mathcal{U}(\boldsymbol{\theta})\,|\phi\rangle\,\big) \ , \quad (8)$$

where $|\partial_{\theta_k}\psi(\boldsymbol{\theta})\rangle = -\frac{i}{2}\mathcal{W}(\boldsymbol{\theta})\,|\phi\rangle$. In what follows, we simplify the notations of the quantum circuits as $\mathcal{U} = \mathcal{U}(\boldsymbol{\theta})$ and $\mathcal{W} = \mathcal{W}(\boldsymbol{\theta})$.

The scalar $\Re\big(\,\langle\phi|\,\mathcal{W}^\dagger\mathcal{H}\mathcal{U}\,|\phi\rangle\,\big)$ is obtained in a similar way as in the second quantization case, namely with the circuit of Eq. (6) but by measuring both the ancilla qubit (in the computational basis) and the variational state register. This is given by the following quantum circuit,

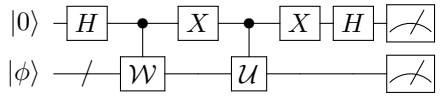

We prove this by first considering the potential part of the Hamiltonian. In this case, $\langle\phi|\,\mathcal{W}^\dagger\mathcal{V}\mathcal{U}\,|\phi\rangle$ is calculated from $\mathbb{E}[(-1)^s\mathcal{V}(j)]$ where s is the measurement outcome of the ancilla qubit, while j is that of the register. Indeed, the probability of measuring states s and j from the above circuit is

$$\begin{aligned} p(s,j) &= \big|\,\langle s,j|\,\big(\,|-\rangle\langle-|\otimes\mathcal{W} + |+\rangle\langle+|\otimes\mathcal{U}\big)\,|0,\phi\rangle\,\big|^2 \\ &= \frac{1}{4}\big|\,\langle j|\,\mathcal{U}\,|\phi\rangle + (-1)^s\,\langle j|\,\mathcal{W}\,|\phi\rangle\,\big|^2 \\ &= \frac{1}{4}\Big(|\,\langle j|\,\mathcal{U}\,|\phi\rangle\,|^2 + |\,\langle j|\,\mathcal{W}\,|\phi\rangle\,|^2 \\ &\qquad + 2(-1)^s\Re\big(\,\langle\phi|\,\mathcal{W}^\dagger\,|j\rangle\,\langle j|\,\mathcal{U}\,|\phi\rangle\,\big)\Big) \ . \end{aligned} \quad (9)$$

With this, we finally obtain

$$\begin{aligned} \mathbb{E}[(-1)^s\mathcal{V}(j)] &= \sum_{s,j}(-1)^s\mathcal{V}(j)p(s,j) \\ &= \sum_j \mathcal{V}(j)\Re\big(\,\langle\phi|\,\mathcal{W}^\dagger\,|j\rangle\,\langle j|\,\mathcal{U}\,|\phi\rangle\,\big) \\ &= \Re(\langle\phi|\,\mathcal{W}^\dagger\mathcal{V}\mathcal{U}\,|\phi\rangle) \ . \end{aligned} \quad (10)$$

The same can be shown for the kinetic part of the Hamiltonian, provided the register is measured in the momentum basis, i. e., by introducing a QFT before the measurement.

Note that the encoding (real space discretization on a grid) employed here is different from the discrete variable representation (DVR) of Ref. 65. We argue in favor of the present grid encoding as the DVR representation leads to an exponentially growing number of Hamiltonian terms.

C. Wavefunction representation and quantum advantage

The quantum advantage of the approach presented herein relies on the possibility to accurately approximate the wavefunction with a quantum computer, using a number of variational parameters that is much smaller than the size of the full Hilbert space. The number of measurements to get the necessary expectation values for M_{kj} and V_k of Eqs. (3)-(4) is given by the number of terms in the Hamiltonian. This is an advantage over classical algorithms where the cost of computing those expectation values is dictated by the more costly wavefunction representation.

The parameters can then be propagated efficiently according to Eq. (2), as long as the number of parameters scales favorably (i.e., polynomially) with the system size. In this case, the system dynamics can be accurately described on a low-dimensional submanifold of the full Hilbert space by a suitable variational wavefunction, which can be efficiently implemented as a quantum circuit.

When working in the first quantization framework, the translation of a Trotter operator $\mathcal{T}$ into a quantum circuit can be very costly in terms of the gate count. Indeed, an efficient decomposition of $\mathcal{T} = \exp(-i\mathcal{V}(\boldsymbol{r})t)$ for an arbitrary potential energy function $\mathcal{V}(\boldsymbol{r})$ into a set of quantum gates is not guaranteed to exist. In fact, the quantum circuit for encoding a general function requires either exponentially many gates or ancilla qubits to perform quantum arithmetic. In the latter case, the targeted function is generally approximated and the number of ancilla qubits scales exponentially with the inverse of the desired accuracy [45, 48, 49, 66].

On one hand, this speaks in favor of the use of variational approaches for time-propagation over Trotter-based algorithms since the former does not require the implementation of an accurate (and costly) gate decomposition of the operator $\mathcal{T}$. On the other hand, finding appropriate, physically motivated, variational *Ansätze* is still a challenge, and heuristic, hardware efficient approaches are therefore often preferred. Hence, as a first demonstration in low dimensions, we will limit ourselves to heuristic variational forms, which can be implemented on quantum hardware. These can be systematically improved by repeating the same quantum circuit units with independent parameters, i. e., by increasing the circuit depth d. The different heuristic circuits employed in this work are detailed in the Supplemental Material.

III. RESULTS

In this section, we study the performance of the quantum algorithm for concrete applications in first quantization. We seek to perform this study without introducing any quantum hardware noise bias, e. g., gate infidelities, relaxation time, or statistical sampling. Hence, the simulations are obtained in a perfect classical emulator of a quantum computer. The expectation values are computed from matrix-vector multiplications. For this reason, we approximate the wavefunction derivatives with forward finite differences of step-size 10^{-8}. We show in the Supplemental Material that this step-size leads to converged results. The equations of motion (Eq. (2)) are solved with a least-squares approach as implemented in NumPy [67] with a cutoff ratio for small singular values, or reconditioning number, arbitrarily set to 10^{-6}. To solve the ordinary differential equations, we employ a state-of-the-art adaptive Runge-Kutta solver of order 5(4) available in SciPy-routines [2].

A. Position and momentum spaces

We first test the VTE approach in one-dimensional systems defined on a grid as described in Ref. [45] and in the Supplemental Material. The length of the box is L = 14. We study three different problems: a freely moving particle, a particle in a harmonic potential (harmonic oscillator), and a particle colliding with an Eckart barrier. The Hamiltonians for these three systems are given by

$$\mathcal{H}_{\mathrm{FP}} = \frac{1}{2m}p^2 \ , \tag{11}$$

$$\mathcal{H}_{\mathrm{HO}} = \frac{1}{2m}p^2 + c_1 x^2 \ , \tag{12}$$

$$\mathcal{H}_{\mathrm{EB}} = \frac{1}{2m}p^2 + \frac{c_2}{\cosh^2(c_3 x)} \ . \tag{13}$$

We work in atomic units, taking $m = 1$, $c_1 = 1$, $c_2 = 13$, and $c_3 = 3/2$. In all cases, the state is initialized to a Gaussian wavepacket,

$$\psi_0(x) = \frac{1}{\mathcal{A}} \exp\left(-\frac{1}{4}\left(\frac{x - x_0}{\mathcal{B}}\right)^2\right) \exp(ip_0 x) \ , \tag{14}$$

with $\mathcal{A}$ the normalization factor, $\mathcal{B}$ the width of the wavepacket, and p_0 and x_0 the initial momentum and position, respectively. The evolution is carried out for a total time $t_{\mathrm{tot}} = 1.5$. Snapshots of the exact time evolution (from exact exponentiation of the Hamiltonian matrix) for each of the three systems are shown in Figs. 1a-c for times $t = 0, 0.45, 0.91$, and 1.5.

The space is discretized with $N_q = 6$ qubits (corresponding to 64 grid points). In this case, the full Hilbert space can be described by $n_p^{\mathrm{full}} = 2(2^6 - 1) = 126$ real parameters. It is clear that a quantum advantage can only be achieved with a much smaller number of variational parameters, satisfying $n_p \ll n_p^{\mathrm{full}}$. We perform VTE simulations for each of the three aforementioned systems with the variational form vf1 (see Supplemental Material) for different depths (or circuit repetitions, see Supplemental Material). Consistent with Eq. (1), we denote the variational form by $\mathcal{U}(\boldsymbol{\theta})$.

The initial parameters $\boldsymbol{\theta}_0$ are found by maximizing the fidelity $\mathcal{F}(t = 0) = |\langle\psi_0|\mathcal{U}(\boldsymbol{\theta}_0)|0\rangle|^2$, where $|0\rangle$ is the vacuum state. The initial conditions are $(x_0, p_0) = (-3.5, 5)$

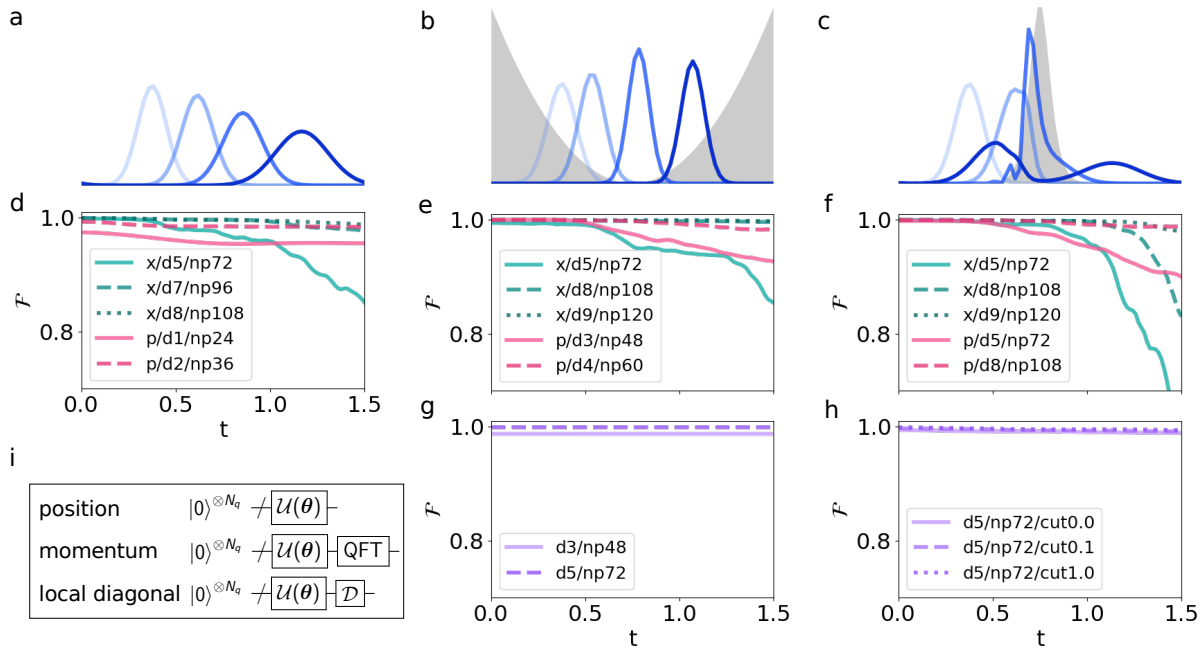

FIG. 1. VTE dynamics for the three one-dimensional systems considered in this study.
top panels Snapshots of the modulus square of the exact wavefunctions at times $t = 0.00, 0.45, 0.91$, and 1.5 for a) the free particle, b) the harmonic oscillator, c) the Eckart barrier.
middle panels Fidelity, $\mathcal{F}$ as a function of time, t, of the VTE dynamics in position (x) and momentum (p) space for d) the free particle, e) the harmonic oscillator, f) the Eckart barrier. The results are obtained with 6 qubits and variational form vf1 at depth d (with corresponding number n_p of variational parameters).
bottom panels Fidelity, $\mathcal{F}$ as a function of time, t, of the VTE in LD space for g) the harmonic oscillator, h) the Eckart barrier. The results are obtained with 6 qubits and variational form vf2 at depth d (with corresponding number n_p of variational parameters). In the case of the Eckart barrier, the fidelity results are given for different cutoffs, *cut*, of the Hamiltonian coefficients used to obtain the diagonalization unitary (see main text). Panel i) shows the different quantum circuits employed in position, moment, and diagonal space.

for the free particle and the Eckart barrier, and $(x_0, p_0) = (-3.5, 2)$ for the harmonic oscillator. In all cases, the width of the initial wavepacket is set to $\mathcal{B} = 1/\sqrt{2}$.

The fidelities $\mathcal{F}(t) = |\langle\psi_0|e^{i\mathcal{H}t}\mathcal{U}(\boldsymbol{\theta}(t))|0\rangle|^2$, as a function of the simulation time, are shown in Fig. 1d-e. These results demonstrate that, in general, the number of variational parameters required to maintain a fidelity above 95% throughout the entire simulation time always approaches n_p^{full}, particularly so when tackling hard problems such as the scattering on the Eckart barrier, quenching the potential for quantum advantage. The evolution of all parameters is also given in the Supplemental Material and shows sharp changes in their trajectories for each of the three systems. To our understanding, supported by the detailed study given in the Supplemental Material, the above observations can be rationalized as follows. The chosen heuristic variational forms have enough flexibility to accurately and efficiently, i. e., with few variational parameters, approximate the targeted wavefunctions at all times of their dynamics. Therefore, the loss of accuracy observed throughout the different simulations is not due to the variational forms, but is an inherent effect of the VTE. When the number of variational parameters is insufficient, the dynamics strongly depends on the numerical setup of the simulation (grid mesh, reconditioning number, initial parameters, etc.). These observations are in agreement with Ref. 65 where strong numerical instabilities were also put forward. Surprisingly, the correct dynamics are always recovered when increasing the number of variational parameters. In this case, the algorithm is stable. In addition, we observe that the more complex the dynamics get, the more parameters are needed.

We repeated our simulations in the momentum representation by defining a variational *Ansatz* of the form $\mathcal{U}_p(\boldsymbol{\theta}) = \text{QFT}\,\mathcal{U}(\boldsymbol{\theta})$ (see also Fig. 1i). The results are given in Fig. 1d-f. As expected, the evolution of the free particle can now be performed accurately with very few parameters, since the introduced momentum basis diagonalizes the Hamiltonian. Interestingly however, the evolution is also smoother in the case of the harmonic oscillator and the Eckart barrier. Note that we do not expect the harmonic oscillator to be symmetric in position and momentum representations, since the position and momentum grids are different and the corresponding potentials come with different prefactors. In the Supplemental Material, we show that this momentum space

representation improves the dynamics compared to the position space in all cases considered in this work. Results obtained by combining both the position and the momentum representation in a common *Ansatz* are also given in the Supplemental Material but do not show substantial improvements.

In order to search for efficient heuristic *Ansätze*, we systematically change the characteristics of the variational circuit, namely the single-qubit rotations, the type of entangling gates, and the connectivity of the entangling block (see Supplemental Material for details). We apply all these different variational forms to the simulation of the wavepacket interacting with the Eckart barrier. The results presented in the Supplemental Material show that, in general, the accuracy is improved by working in the momentum representation and increasing the circuit depth. However, no clear trend for the design of more efficient variational forms could be identified.

B. Local diagonal space

The introduction of unitary transformations that achieve a (at least partial) diagonalization of the Hamiltonian seems essential to make the quantum VTE efficient in the grid representation. As a demonstration of this strategy, we first classically diagonalize the harmonic oscillator and Eckart barrier Hamiltonians. We then map the unitary matrix, made up of the eigenvectors sorted by increasing order of energy, to a quantum circuit using the isometry decomposition of Ref. 69 as implemented in Qiskit [70]. The resulting circuits $\mathcal{D}$ are then appended to the variational form as shown in Fig. 1i. To obtain the results of Fig. 1g-h, we add $\mathcal{D}$ to the variational form vf2 (see Supplemental Material). Those results show a high state fidelity over the entire simulation time. In the case of the Eckart potential, we also tested unitaries $\mathcal{D}'$, which only perform a partial diagonalization of the Hamiltonian. More specifically, prior to diagonalization, we set to zero all matrix elements with absolute values below cutoff thresholds of $cut = 0.1$ and 1.0. The density of non-zero elements in the resulting Hamiltonian matrix is then 0.98, 0.27, and 0.14 for cutoffs 0, 0.1, and 1.0, respectively. The results exhibit high accuracy for all cutoff values as seen from Fig. 1h.

These preliminary tests demonstrate the potential of the diagonalization step following the application of the variational form. Of more interest is the application of this approach to multidimensional systems. In particular, we see that an approximate diagonalization of the system Hamiltonian can already give a sufficiently accurate and stable time evolution. This suggests that, for a multi-dimensional configuration space, an improvement can already be achieved by diagonalizing each dimension independently, i. e., by fixing all but one coordinate of the Hamiltonian. This leads to a quantum circuit of the form

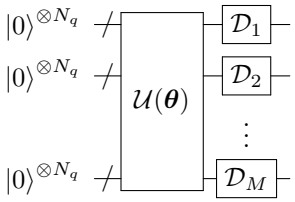

(15)

We call the space obtained from this basis transformation the local diagonal (LD) space. In the next paragraph, we discuss the scaling of this approach.

As stated earlier, we employ N grid points, corresponding to $N_q = \log_2(N)$ qubits, for each of the M dimensions. Hence, the total number of qubits is MN_q. The total size of the problem is N^M, prohibitively large for direct classical simulations in high dimensions. Efficient algorithms should scale to low polynomial order in N and M. Our approach first requires the diagonalization of M matrices of size (N, N). This step generally scales as $\mathcal{O}(N^3)$. The resulting unitary is then translated into a quantum circuit. The classical scaling of this operation is $\mathcal{O}(N_q N^3)$ [71], leading to $\mathcal{O}(N^2)$ CNOT gates [69]. Finally, the VTE is performed with a variational form comprising n_p parameters. The partial diagonalization step ensures the scaling of n_p to be of low polynomial order, i. e., $\mathcal{O}\big((MN_q)^P\big)$ where P is small enough such that $(MN_q)^P \ll N^M$. At each time step of the VTE, the equations of motion are reconstructed with $\mathcal{O}(n_p^2)$ measurements and solved classically at cost $\mathcal{O}\big(n_p^3\big)$. Recent approaches such as the one of Ref. 72 focus on reducing the scaling in n_p for obtaining the M matrix and could be extended to the present case. Finally, we obtain an efficient hybrid quantum-classical time evolution algorithm with polynomial scaling in N and M.

As a proof of concept, we test this approach on the evolution of a two-dimensional system on a *Mexican Hat* potential energy surface (PES). The Hamiltonian reads

$$\mathcal{H}_{\mathrm{MH}} = \frac{1}{2m}(p_x^2 + p_y^2) + c_4 r^4 - c_5 r^2 \ , \tag{16}$$

with $r^2 = x^2 + y^2$, $c_4 = 0.1$, $c_5 = 1$, and again $m = 1$. The space is discretized with 8 qubits (4 per dimension), corresponding to a total of 256 grid points. Note that the Hilbert space can be fully represented by 510 real parameters. The wavepacket is evolved in the region of space $x \in [-5, 5]$ and $y \in [-5, 5]$. It is initialized at $(x_0, y_0) = (-3.0, 0)$ with no initial momentum and width $\sigma_x = \sigma_y = 1$. The momentum increases in subsequent time steps as the wavepacket slides down the brim of the PES. A graphical representation of the system is given in Fig. 2a together with snapshots of the exact evolution for times $t = 0, 0.91, 1.8$, and 3.0.

We simulate the quantum dynamics with VTE up to $t_{\mathrm{tot}} = 3.0$, employing the same settings as before, and using both the position and the LD *Ansatz*. The one-dimensional Hamiltonians $\mathcal{H}_x = \mathcal{H}(x, 0)$ and $\mathcal{H}_y = \mathcal{H}(0, y)$ are diagonalized to get the quantum circuits $\mathcal{D}_x$

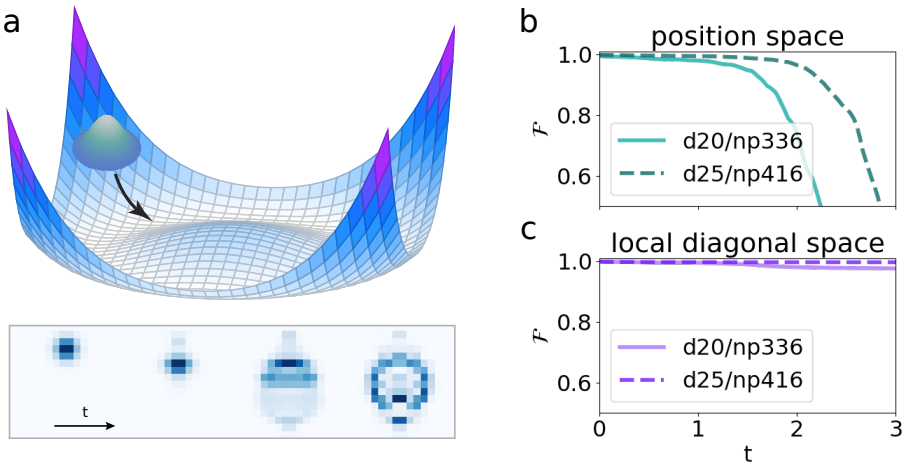

FIG. 2. VTE dynamics of a two-dimensional system, representing a wavepacket evolving on a "mexican hat" potential.
a) 3-dimensional representation of the system at the top and, at the bottom, snapshots of the modulus square of the exact wavefunction at times $t = 0.00, 0.91, 1.8$, and 3.0.
Beside are the results of the VTE dynamics obtained in b) the position space and c) the LD space. The fidelity, $\mathcal{F}$ as a function of time, t, is obtained with 8 qubits and variational form vf1 at depth d (with the corresponding number n_p of variational parameters).

and $\mathcal{D}_y$. For both the evolutions in position and LD space, the parameterized part of the quantum circuit $\mathcal{U}(\boldsymbol{\theta})$ corresponds to the variational form vf1 with depth 20 and depth 25 (336 and 416 parameters, respectively). The results are displayed in Fig. 2b and c. Significant improvements are obtained in diagonal space. Note that these results were obtained from a choice of one-dimensional Hamiltonians that are very simple to diagonalize. They could be improved even further by exploiting symmetries of the system or by diagonalizing low-dimensional mean-field Hamiltonians.

IV. CONCLUSIONS

In this paper, we introduced a quantum VTE algorithm to perform nuclear wavepacket dynamics on a grid in first quantization.

The potential quantum advantage of the present approach resides in the favourable scaling in the computational resource (number of qubits), which grows only logarithmically with the number of grid points considered. In addition, the variational algorithm manifests a crucial advantage compared to Trotter-like quantum approaches to this problem class, namely the fact that it does not require the direct implementation of the time-evolution operator (exponentiating the Hamiltonian) in the qubit register. This is of paramount importance as constructing such a circuit for Hamiltonians in first quantization is a very unpractical and resource demanding task. Furthermore, we stressed the advantage of our method in relation to the need of sampling expectations values in only two bases representations (position and momentum), irrespective of the system size. In fact, this constitutes an important advantage compared to previous implementations of the same VTE quantum algorithm, e. g., in second quantization or in the DVR representation. This is of particular relevance knowing that the high number of measurements required to perform the VTE becomes quickly impractical when increasing the dimensionality of the problem [62, 72, 73].

We studied the performance of the quantum algorithm in classical emulations for several one- and two-dimensional systems. In general, we observed strong numerical instabilities when performing the dynamics with a minimal number of variational parameters. In fact, the number of parameters needed to maintain the required accuracy throughout the dynamics often approaches the size of the full Hilbert space, hampering any potential quantum advantage. However, we could demonstrate that the accuracy and efficiency of the quantum algorithm can be further improved by expressing the variational quantum circuit in a problem specific basis. This basis is obtained by diagonalizing each dimension of the system independently, without introducing significant computational overhead. We discussed the overall cost of the proposed approach, which shows an effective polynomial scaling in both the number of grid points per dimension, N, and the number of system dimensions, M (for a total of N^M grid points).

In conclusion, the quantum dynamics algorithm introduced in this paper constitutes an important step forward in the efficient simulation of the dynamics of complex, multidimensional quantum systems with near-term, noisy, quantum computers. These are notoriously hard to simulate classically due to the exponential scaling of the

resources, offering therefore an ideal playground to showcase quantum advantage. Furthermore, our approach can be easily extended to the simultaneous treatment of electronic and nuclear degrees of freedom, opening up new opportunities for the simulation of non-adiabatic dynamics beyond the Born-Oppenheimer approximation.

V. ACKNOWLEDGEMENTS

The authors thank Christa Zoufal for useful discussions and acknowledge financial support from the Swiss National Science Foundation (SNF) through the grant No. 200021-179312.

[1] F. Gatti, *Molecular quantum dynamics: from theory to applications* (Springer, 2014).
[2] R. J. McMahon, Science **299**, 833 (2003).
[3] B. Stuart, Kirk-Othmer encyclopedia of chemical technology (2000).
[4] B. D. Ravetz, A. B. Pun, E. M. Churchill, D. N. Congreve, T. Rovis, and L. M. Campos, Nature **565**, 343 (2019).
[5] A. H. Zewail, in *Femtochemistry: Ultrafast Dynamics of the Chemical Bond: Volume I* (World Scientific, 1994) pp. 3–22.
[6] H. Ihee, V. A. Lobastov, U. M. Gomez, B. M. Goodson, R. Srinivasan, C.-Y. Ruan, and A. H. Zewail, Science **291**, 458 (2001).
[7] M. Drescher, M. Hentschel, R. Kienberger, M. Uiberacker, V. Yakovlev, A. Scrinzi, T. Westerwalbesloh, U. Kleineberg, U. Heinzmann, and F. Krausz, Nature **419**, 803 (2002).
[8] E. Goulielmakis, Z.-H. Loh, A. Wirth, R. Santra, N. Rohringer, V. S. Yakovlev, S. Zherebtsov, T. Pfeifer, A. M. Azzeer, M. F. Kling, *et al.*, Nature **466**, 739 (2010).
[9] F. Krausz and M. Ivanov, Reviews of Modern Physics **81**, 163 (2009).
[10] H. Tal-Ezer and R. Kosloff, The Journal of Chemical Physics **81**, 3967 (1984).
[11] C. Lanczos, *An iteration method for the solution of the eigenvalue problem of linear differential and integral operators*, Vol. 45 (United States Governm. Press Office Los Angeles, CA, 1950) pp. 255–282.
[12] M. Feit, J. Fleck Jr, and A. Steiger, Journal of Computational Physics **47**, 412 (1982).
[13] M. Feit and J. Fleck Jr, The Journal of Chemical Physics **78**, 301 (1983).
[14] R. Kosloff, The Journal of Physical Chemistry **92**, 2087 (1988).
[15] N. K. Madsen, M. B. Hansen, G. A. Worth, and O. Christiansen, Journal of Chemical Theory and Computation **16**, 4087 (2020).
[16] W. H. Miller, Proceedings of the National Academy of Sciences **102**, 6660 (2005).
[17] R. B. Gerber, V. Buch, and M. A. Ratner, The Journal of Chemical Physics **77**, 3022 (1982).
[18] R. Gerber and M. A. Ratner, Advances in Chemical Physics **70**, 97 (1988).
[19] H.-D. Meyer, U. Manthe, and L. S. Cederbaum, Chemical Physics Letters **165**, 73 (1990).
[20] M. H. Beck, A. Jäckle, G. A. Worth, and H.-D. Meyer, Physics Reports **324**, 1 (2000).
[21] I. Burghardt, K. Giri, and G. Worth, The Journal of Chemical Physics **129**, 174104 (2008).
[22] H. Wang and M. Thoss, The Journal of Chemical Physics **119**, 1289 (2003).
[23] H. Wang and M. Thoss, The Journal of Chemical Physics **131**, 024114 (2009).
[24] U. Manthe, The Journal of Chemical Physics **128**, 164116 (2008).
[25] O. Vendrell and H.-D. Meyer, The Journal of Chemical Physics **134**, 044135 (2011).
[26] F. Di Maiolo, G. A. Worth, and I. Burghardt, The Journal of Chemical Physics **154**, 144106 (2021).
[27] N. K. Madsen, M. B. Hansen, G. A. Worth, and O. Christiansen, The Journal of Chemical Physics **152**, 084101 (2020).
[28] G. A. Worth and I. Burghardt, Chemical Physics Letters **368**, 502 (2003).
[29] G. Richings, I. Polyak, K. Spinlove, G. Worth, I. Burghardt, and B. Lasorne, International Reviews in Physical Chemistry **34**, 269 (2015).
[30] R. Martinazzo, M. Nest, P. Saalfrank, and G. F. Tantardini, The Journal of Chemical Physics **125**, 194102 (2006).
[31] D. V. Shalashilin and M. S. Child, The Journal of Chemical Physics **115**, 5367 (2001).
[32] J. A. Green, A. Grigolo, M. Ronto, and D. V. Shalashilin, The Journal of Chemical Physics **144**, 024111 (2016).
[33] T. J. Martínez and R. Levine, Journal of the Chemical Society, Faraday Transactions **93**, 941 (1997).
[34] B. F. Curchod and T. J. Martínez, Chemical Reviews **118**, 3305 (2018).
[35] H. Weir, M. Williams, R. M. Parrish, E. G. Hohenstein, and T. J. Martínez, The Journal of Physical Chemistry B **124**, 5476 (2020).
[36] R. P. Feynman, International Journal of Theoretical Physics **21** (1999).
[37] F. Tacchino, A. Chiesa, S. Carretta, and D. Gerace, Advanced Quantum Technologies **3**, 1900052 (2020).
[38] S. Wiesner, arXiv preprint quant-ph/9603028 (1996).
[39] C. Zalka, Proceedings of the Royal Society of London. Series A: Mathematical, Physical and Engineering Sciences **454**, 313 (1998).
[40] Y. Fan, International Journal of Quantum Information **10**, 1250049 (2012).

[41] G. Benenti and G. Strini, American Journal of Physics **76**, 657 (2008).
[42] R. D. Somma, arXiv preprint arXiv:1503.06319v2 (2015).
[43] M. Ostrowski, Bulletin of the Polish Academy of Sciences. Technical Sciences **63**, 379 (2015).
[44] A. Macridin, P. Spentzouris, J. Amundson, and R. Harnik, Physical Review Letters **121**, 110504 (2018).
[45] P. J. Ollitrault, G. Mazzola, and I. Tavernelli, Phys. Rev. Lett. **125**, 260511 (2020).
[46] P. J. Ollitrault, A. Miessen, and I. Tavernelli, Accounts of Chemical Research **54**, 4229 (2021).
[47] D. W. Berry, G. Ahokas, R. Cleve, and B. C. Sanders, Communications in Mathematical Physics **270**, 359 (2007).
[48] S. Woerner and D. J. Egger, npj Quantum Information **5**, 1 (2019).
[49] T. Häner, M. Roetteler, and K. M. Svore, (2018), arXiv:1805.12445 [quant-ph].
[50] I. Kassal, S. P. Jordan, P. J. Love, M. Mohseni, and A. Aspuru-Guzik, Proceedings of the National Academy of Sciences **105**, 18681 (2008).
[51] H. H. S. Chan, R. Meister, T. Jones, D. P. Tew, and S. C. Benjamin, (2022), arXiv:2202.05864 [quant-ph].
[52] N. C. Jones, J. D. Whitfield, P. L. McMahon, M.-H. Yung, R. V. Meter, A. Aspuru-Guzik, and Y. Yamamoto, New Journal of Physics **14**, 115023 (2012).
[53] X. Yuan, S. Endo, Q. Zhao, Y. Li, and S. C. Benjamin, Quantum **3**, 191 (2019).
[54] M. Cerezo, A. Arrasmith, R. Babbush, S. C. Benjamin, S. Endo, K. Fujii, J. R. McClean, K. Mitarai, X. Yuan, L. Cincio, *et al.*, Nature Reviews Physics **3**, 625 (2021).
[55] Y. Li and S. C. Benjamin, Physical Review X **7**, 021050 (2017).
[56] L. Hackl, T. Guaita, T. Shi, J. Haegeman, E. A. Demler, and J. I. Cirac, SciPost Physics **9** (2020).
[57] Y.-X. Yao, N. Gomes, F. Zhang, C.-Z. Wang, K.-M. Ho, T. Iadecola, and P. P. Orth, PRX Quantum **2**, 030307 (2021).
[58] N. Gomes, A. Mukherjee, F. Zhang, T. Iadecola, C.-Z. Wang, K.-M. Ho, P. P. Orth, and Y.-X. Yao, Advanced Quantum Technologies **4**, 2100114 (2021).
[59] S. McArdle, T. Jones, S. Endo, Y. Li, S. C. Benjamin, and X. Yuan, npj Quantum Information **5**, 1 (2019).
[60] M. Schuld, V. Bergholm, C. Gogolin, J. Izaac, and N. Killoran, Phys. Rev. A **99**, 032331 (2019).
[61] S. McArdle, S. Endo, A. Aspuru-Guzik, S. C. Benjamin, and X. Yuan, Review of Modern Physics **92**, 015003 (2020).
[62] A. Miessen, P. J. Ollitrault, and I. Tavernelli, Physical Review Research **3**, 043212 (2021).
[63] R. Somma, G. Ortiz, J. E. Gubernatis, E. Knill, and R. Laflamme, Physical Review A **65**, 042323 (2002).
[64] U. Manthe, Quantum Simulations of Complex Many-Body Systems: From Theory to Algorithms, Lecture Notes.—Jülich: John von Neumann Institute for Computing , 361 (2002).
[65] C.-K. Lee, C.-Y. Hsieh, S. Zhang, and L. Shi, arXiv preprint arXiv:2110.06143 (2021).
[66] K. Mitarai, M. Kitagawa, and K. Fujii, Physical Review A **99**, 012301 (2019).
[67] C. R. Harris, K. J. Millman, S. J. van der Walt, R. Gommers, P. Virtanen, D. Cournapeau, E. Wieser, J. Taylor, S. Berg, N. J. Smith, R. Kern, M. Picus, S. Hoyer, M. H. van Kerkwijk, M. Brett, A. Haldane, J. F. del Río, M. Wiebe, P. Peterson, P. Gérard-Marchant, K. Sheppard, T. Reddy, W. Weckesser, H. Abbasi, C. Gohlke, and T. E. Oliphant, Nature **585**, 357 (2020).
[2] P. Virtanen, R. Gommers, T. E. Oliphant, M. Haberland, T. Reddy, D. Cournapeau, E. Burovski, P. Peterson, W. Weckesser, J. Bright, S. J. van der Walt, M. Brett, J. Wilson, K. J. Millman, N. Mayorov, A. R. J. Nelson, E. Jones, R. Kern, E. Larson, C. J. Carey, İ. Polat, Y. Feng, E. W. Moore, J. VanderPlas, D. Laxalde, J. Perktold, R. Cimrman, I. Henriksen, E. A. Quintero, C. R. Harris, A. M. Archibald, A. H. Ribeiro, F. Pedregosa, P. van Mulbregt, and SciPy 1.0 Contributors, Nature Methods **17**, 261 (2020).
[69] R. Iten, R. Colbeck, I. Kukuljan, J. Home, and M. Christandl, Phys. Rev. A **93**, 032318 (2016).
[70] G. Aleksandrowicz, T. Alexander, P. Barkoutsos, L. Bello, Y. Ben-Haim, D. Bucher, F. J. Cabrera-Hernádez, J. Carballo-Franquis, A. Chen, C.-F. Chen, J. M. Chow, A. D. Córcoles-Gonzales, A. J. Cross, A. Cross, J. Cruz-Benito, C. Culver, S. D. L. P. González, E. D. L. Torre, D. Ding, E. Dumitrescu, I. Duran, P. Eendebak, M. Everitt, I. F. Sertage, A. Frisch, A. Fuhrer, J. Gambetta, B. G. Gago, J. Gomez-Mosquera, D. Greenberg, I. Hamamura, V. Havlicek, J. Hellmers, Ł. Herok, H. Horii, S. Hu, T. Imamichi, T. Itoko, A. Javadi-Abhari, N. Kanazawa, A. Karazeev, K. Krsulich, P. Liu, Y. Luh, Y. Maeng, M. Marques, F. J. Martín-Fernández, D. T. McClure, D. McKay, S. Meesala, A. Mezzacapo, N. Moll, D. M. Rodríguez, G. Nannicini, P. Nation, P. Ollitrault, L. J. O'Riordan, H. Paik, J. Pérez, A. Phan, M. Pistoia, V. Prutyanov, M. Reuter, J. Rice, A. R. Davila, R. H. P. Rudy, M. Ryu, N. Sathaye, C. Schnabel, E. Schoute, K. Setia, Y. Shi, A. Silva, Y. Siraichi, S. Sivarajah, J. A. Smolin, M. Soeken, H. Takahashi, I. Tavernelli, C. Taylor, P. Taylour, K. Trabing, M. Treinish, W. Turner, D. Vogt-Lee, C. Vuillot, J. A. Wildstrom, J. Wilson, E. Winston, C. Wood, S. Wood, S. Wörner, I. Y. Akhalwaya, and C. Zoufal, "Qiskit: An open-source framework for quantum computing," (2019).
[71] R. Iten, O. Reardon-Smith, E. Malvetti, L. Mondada, G. Pauvert, E. Redmond, R. S. Kohli, and R. Colbeck, arXiv preprint arXiv:1904.01072 (2019).
[72] J. Gacon, C. Zoufal, G. Carleo, and S. Woerner, Quantum **5**, 567 (2021).
[73] S. Barison, F. Vicentini, and G. Carleo, Quantum **5**, 512 (2021).

Supplementary Information for: Quantum algorithms for grid-based variational time evolution

I. ONE-ANCILLA QUBIT MEASUREMENT PROCESS

In this section, we recall the verification of the following equation:

$$\langle\phi|\,\mathcal{W}_1^\dagger\mathcal{W}_{2,p}\,|\phi\rangle \equiv$$

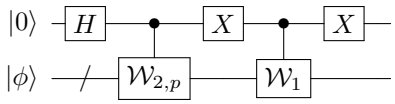

(S1)

The circuit steps can be written as follows:

1. $|\phi\rangle\,|0\rangle \longrightarrow \frac{1}{\sqrt{2}}\,|\phi\rangle\,|0\rangle + \frac{1}{\sqrt{2}}\,|\phi\rangle\,|1\rangle$
2. $\frac{1}{\sqrt{2}}\,|\phi\rangle\,|0\rangle + \frac{1}{\sqrt{2}}\,|\phi\rangle\,|1\rangle \longrightarrow \frac{1}{\sqrt{2}}\,|\phi\rangle\,|0\rangle + \frac{1}{\sqrt{2}}\mathcal{W}_{2,p}\,|\phi\rangle\,|1\rangle$
3. $\frac{1}{\sqrt{2}}\,|\phi\rangle\,|0\rangle + \frac{1}{\sqrt{2}}\mathcal{W}_{2,p}\,|\phi\rangle\,|1\rangle \longrightarrow \frac{1}{\sqrt{2}}\mathcal{W}_1\,|\phi\rangle\,|0\rangle + \frac{1}{\sqrt{2}}\mathcal{W}_{2,p}\,|\phi\rangle\,|1\rangle$
4. Measuring the expectation value of $\sigma_+ = |0\rangle\,\langle 1|$ on the ancilla qubit leads to

$$\langle\sigma_+\rangle = \frac{1}{2}\Big(\,\langle 1|\,\langle\phi|\,\mathcal{W}_{2,p}^\dagger + \langle 0|\,\langle\phi|\,\mathcal{W}_1^\dagger\Big)\,|0\rangle\,\langle 1|\,\Big(\mathcal{U}\,|\phi\rangle\,|0\rangle + \mathcal{W}_{2,p}\,|\phi\rangle\,|1\rangle\Big)\,. \tag{S2}$$

Since $\langle 1|0\rangle = \langle 0|1\rangle = 0$, we obtain

$$\langle\sigma_+\rangle = \frac{1}{2}\,\langle\phi|\,\mathcal{W}_1^\dagger\mathcal{W}_{2,p}\,|\phi\rangle\;\;. \tag{S3}$$

II. HEURISTIC VARIATIONAL FORMS

The different variational forms employed in this work are summarized in Tab. I. They all comprise alternating layers of single qubit rotations and entangling blocks. They differ in the choice of single qubit rotation gates, entangling gates, and coupling map, i. e., in the geometrical way the qubits are coupled to each other. In the linear coupling map, each qubit is coupled to its two nearest neighbors only. The circular map is similar but adds a coupling between the first and last qubits. Finally, in the full coupling map, each qubit is coupled to all other qubits. For the sake of clarity, Fig. S1 gives concrete examples of the resulting circuits for each variational form for four qubits.

Name	Single qubit gates	Entangling gates	Coupling map	# params. for 6 qubits
vf1			linear	depth 5: 72 depth 8: 108
vf2			full	depth 5: 72 depth 8: 108
vf3			circular	depth 5: 72 depth 8: 108
vf4			linear	depth 5: 72 depth 8: 108
vf5	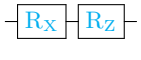		linear	depth 5: 72 depth 8: 108
vf6		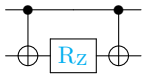	linear	depth 3: 69 depth 5: 103
vf7		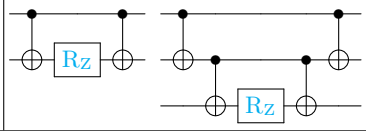	linear	depth 3: 81 depth 4: 102
vf8		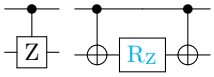	linear	depth 2: 70 depth 8: 99

TABLE I. Definitions of the different variational forms employed throughout this work. The blue colour highlights a parameterized gate. In the last column, we give the number of parameters for the short and long depths circuits used in Section III.

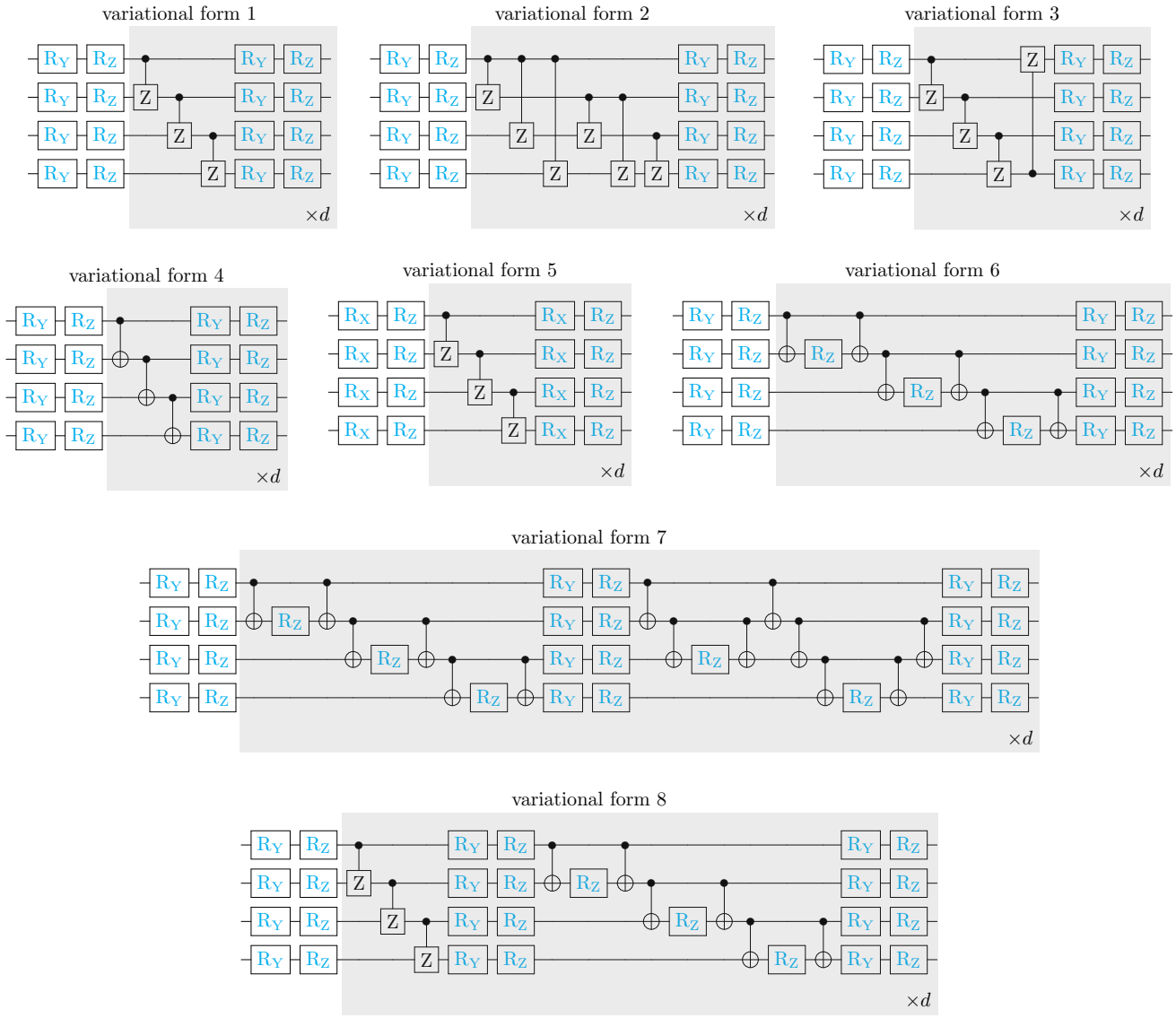

FIG. S1. Quantum circuits for each variational form with depth d on 4 qubits. The blue colour highlights a parameterized gate.

III. COMPARING VARIATIONAL FORMS

One of the main advantages of the variational approach described in this work for first quantized Hamiltonians is the possibility to perform the dynamics without explicitly including the Hamiltonian in the quantum circuit. Instead, heuristic variational forms are exploited. There exist many ways the heuristic variational forms can be defined. Here, we test several ones for the dynamics of the nuclear wavepacket colliding with an Eckart barrier (6 qubits) and compare the resulting fidelities over the simulation time. All variational forms are defined in the first section of this Supplemental Material. From the results shown in Fig. S2 one can see that, in general, an increase in accuracy is obtained by enlarging the depth and by going to momentum space. However, no clear trends can be identified as to how to construct the variational form. Nonetheless, variational forms 1 and 5 (with linear connectivity of controlled-Z entangling gates), seem to generally perform the best.

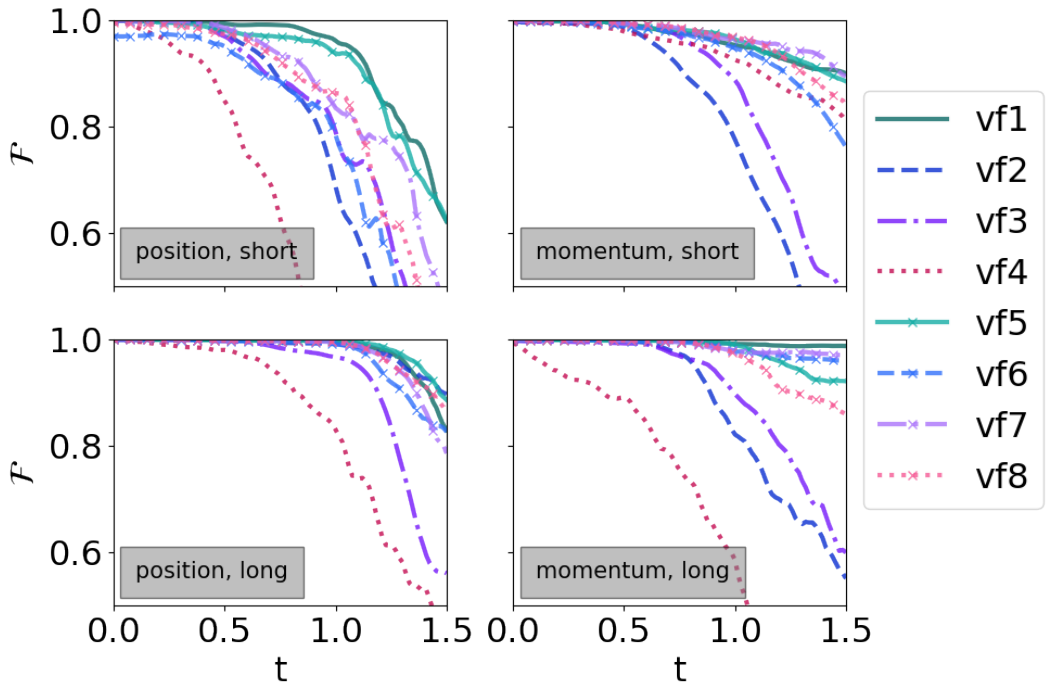

FIG. S2. Fidelity of the variationally time-evolved wavefunction with respect to the exact one as a function of time for *top-left* all variational forms with short depth in position space, *top-right* all variational forms with short depth in momentum space, *bottom-left* all variational forms with large depth in position space and *bottom-left* all variational forms with large depth in momentum space. The specific depths and corresponding number of parameters are given in Tab. I together with the characteristics of each variational form. These results are obtained for the case of the Eckart barrier with 6 qubits.

IV. TIME EVOLUTION OF THE VARIATIONAL PARAMETERS

In this section, we show the dynamics of the parameters obtained with the different VTEs to supplement the fidelity results shown in the main text. In Fig. S3, we report the evolution in position space, in Fig. S4 those in momentum space, and, finally in Fig. S5, the evolutions in local diagonal space. The first two cases (position and momentum) are obtained with variational form vf1, while in the last case (local diagonal), we use variational form vf2.

For all systems, in position space, we observe sharp changes in the dynamics. In general, the parameter values also diverge with time. The same observations can be made in momentum space for the harmonic oscillator and the Eckart barrier.

Whenever the circuit diagonalizes the Hamiltonian as in Fig. S4(a) and Fig. S5(a) and (b), the parameter evolutions become smooth or even trivial. This is unsurprising as, in this case, there is no transfer of amplitudes but only evolution of the phases. Note that in Fig. S5(b), when $cut > 0$, the partial diagonalization of the Hamiltonian suffices to ensure a smoother evolution of the parameters.

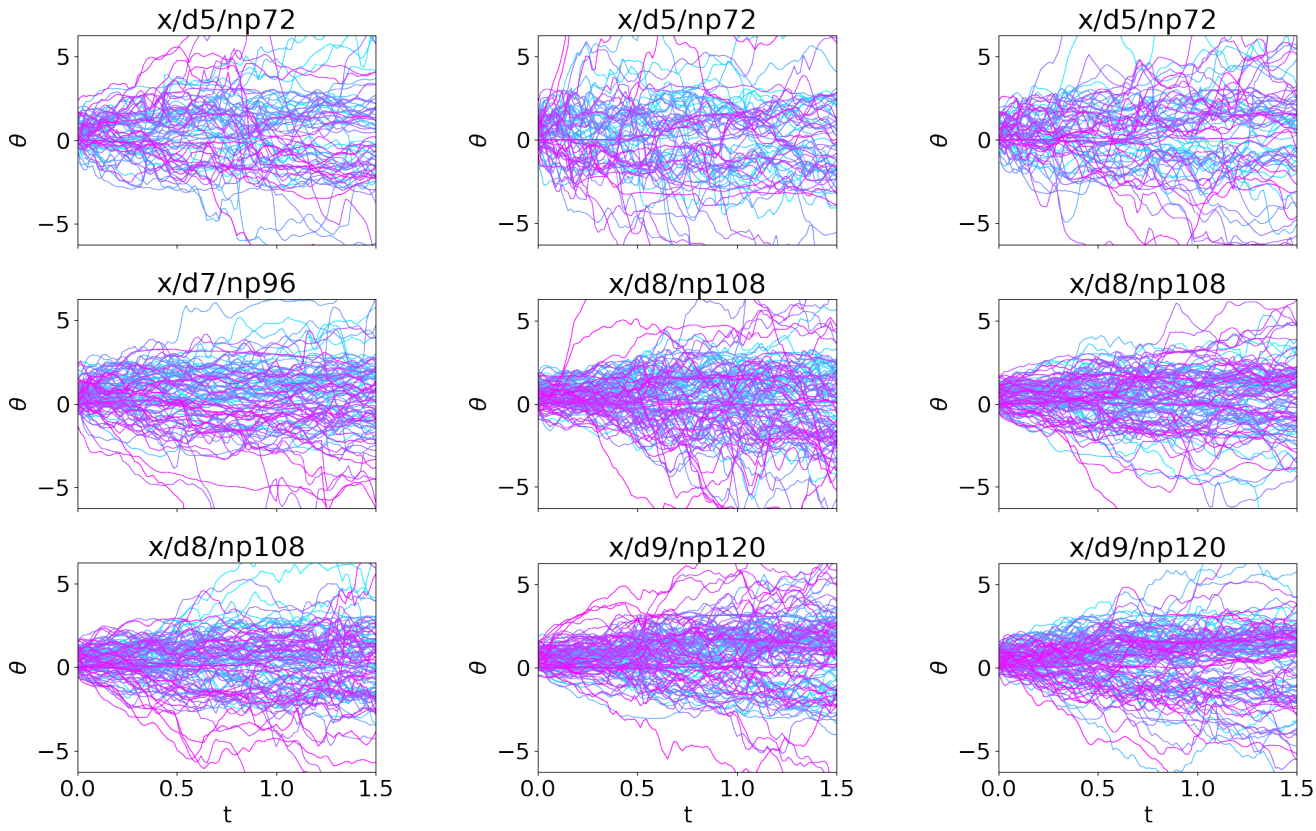

(a) Free particle (b) Harmonic Oscillator (c) Eckart barrier

FIG. S3. Time evolution of the variational parameters for each one-dimensional system obtained with variational form vf1 in position space and at given depth, d (with n_p variational parameters).

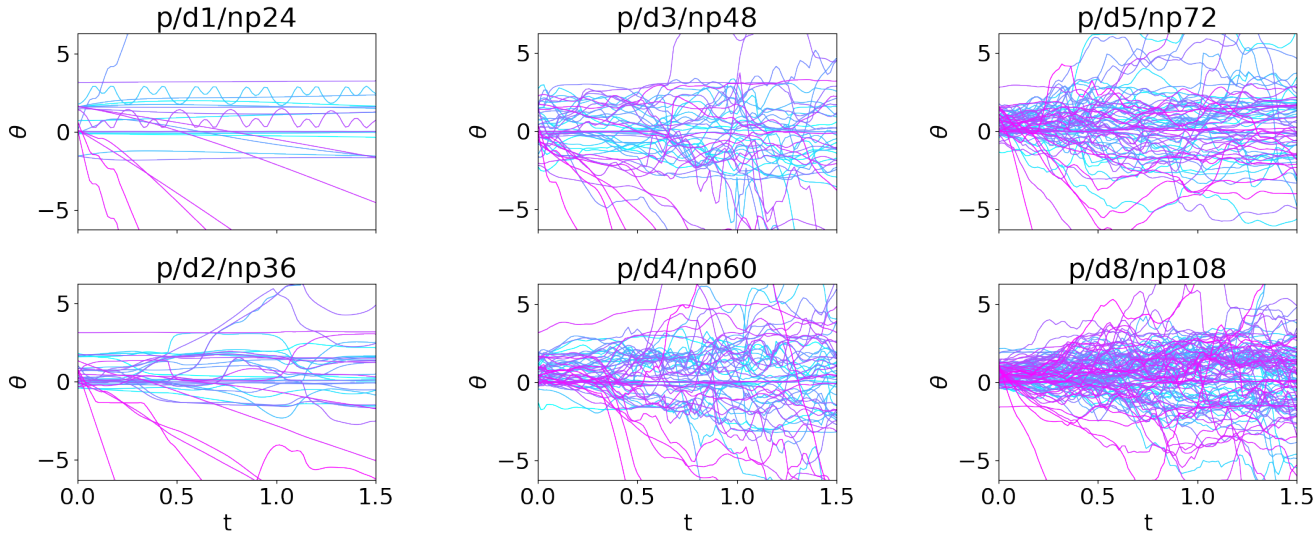

(a) Free particle (b) Harmonic Oscillator (c) Eckart barrier

FIG. S4. Time evolution of the variational parameters for each one-dimensional system obtained with variational form vf1 in momentum space and at given depth, d (with n_p variational parameters).

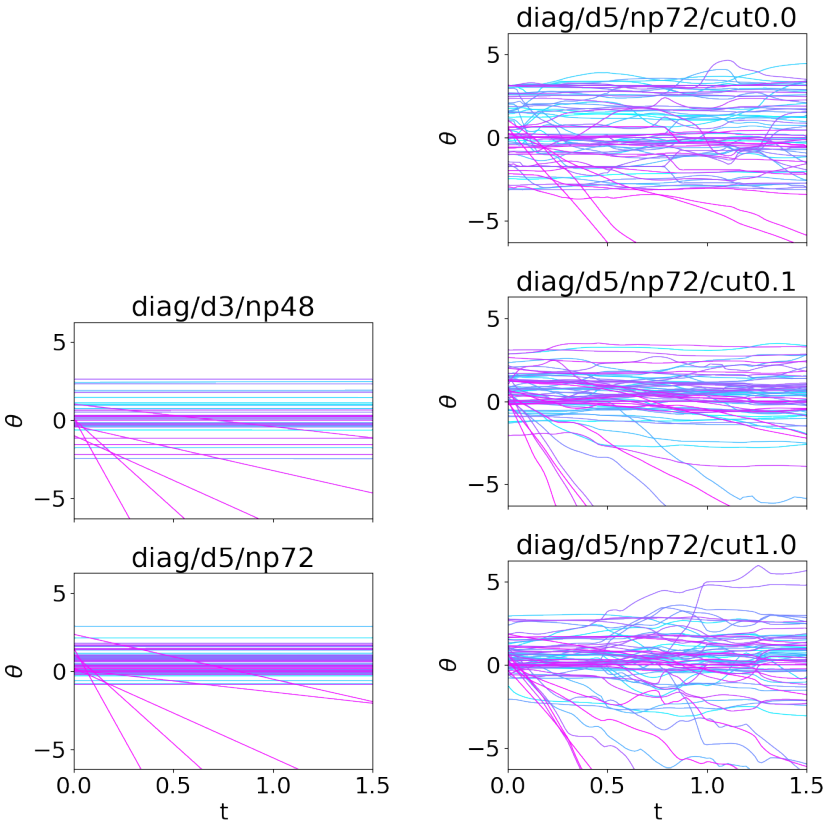

(a) Harmonic Oscillator (b) Eckart barrier

FIG. S5. Time evolution of the variational parameters for two of the one-dimensional systems obtained with variational form vf2 in local diagonal space and at given depth, d (with n_p variational parameters), and cutoff value cut.

V. STUDY ON THE ACCURACY OF THE TIME EVOLUTION IN ONE DIMENSION

To better understand the origin of the errors occurring during the VTE, we perform additional numerical simulations. Unless explicitly stated otherwise, the results of this section are obtained with variational forms in position space.

We start with the Eckart barrier case. The first step is to identify whether the variational form is flexible enough to represent the state at each time step. For this, we optimize the parameters obtained from VTE in 6 qubits with depth 5 and variational form vf1 to maximize $\mathcal{F}(t)$ at each time step (see definition in main text). The results displayed in the top panel of Fig. S6 show that we can indeed get a better fidelity for times $t > 0.8$. This suggests that the variational form is good enough to represent, with good accuracy, the exact wavefunction through the entire dynamics.

There exist several degenerate sets of variational parameters which represent the same wavefunction. In the bottom panel of Fig. S6, we show how the accuracy of the dynamics can be affected by the choice the initial parameters. For the three different trials displayed in Fig. S6, we initialize the parameters by maximizing $\mathcal{F}(t = 0)$. Each one of these three optimization processes is initialized with random parameters and converges to above 99% fidelity. Fig. S6 clearly shows a difference in the fidelities of the dynamics for the three trials. However, we observe that choosing the best set of initial parameters is non-trivial and cannot be made by simply looking at the initial fidelity or early time observables such as the local-in-time error [1].

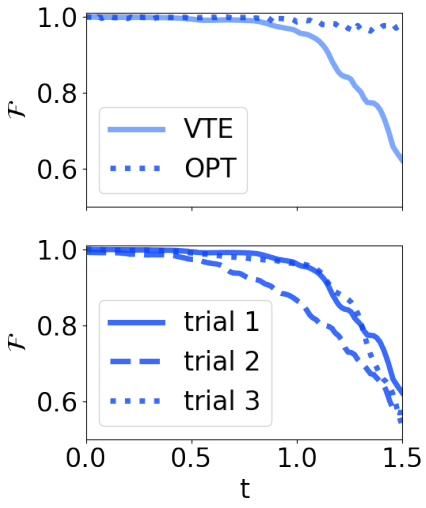

FIG. S6. *Top:* Fidelity of the variationally time-evolved wavefunction with respect to the exact one as a function of time (full line) and after being optimized at each time step to maximize the fidelity (dotted line).
Bottom: Fidelity of the variationally time-evolved wavefunction with respect to the exact one as a function of time for three different sets of initial parameters.
These results are obtained for the case of the Eckart barrier with 6 qubits and variational form vf1, depth 5.

As a second step, we aim to study the effect of the different numerical parameters on the accuracy. We choose to work with the simplest system: a free particle. The space is discretized with 5 qubits. The initial conditions are $(x_0, p_0) = (0, 5)$. The width of the initial wavepacket is set to $\mathcal{B} = 1/\sqrt{2}$. The parametrized circuit corresponds to variational form vf2 with depth 3.

We first run the VTE for different values of the finite difference step size, ϵ. The results are displayed in Fig. S7, showing identical fidelities in the relevant part of the evolution when the accuracy is above 95%.

We then fix ϵ back to its original value of 10^{-8} and change the reconditioning number, rc, the ratio for cutting off small singular values in the least-squares algorithm. The results displayed in Fig. S8 show that the fidelity increases with smaller rc. This implies numerical errors coming from instabilities in the inversion of the matrix M when solving Eq. 2 (main text).

We then study the performance of the ordinary differential equation solver. We employ the same Runge-Kutta 5(4) solver, but now fix the maximum time step to 10^{-4}, and compare to an explicit Runge-Kutta solver of order 8 (DOP853) [2]. As shown in Fig. S9, the results of these two simulations are identical in the first part of the dynamics (before the accuracy drops below 90%) and differ afterwards.

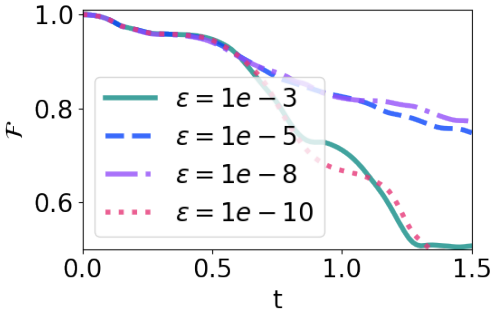

FIG. S7. Fidelity of the variationally time-evolved wavefunction with respect to the exact one as a function of time and for different values of the finite difference step, ϵ. These results are obtained for the case of the free particle with 5 qubits and variational form vf2, depth 3.

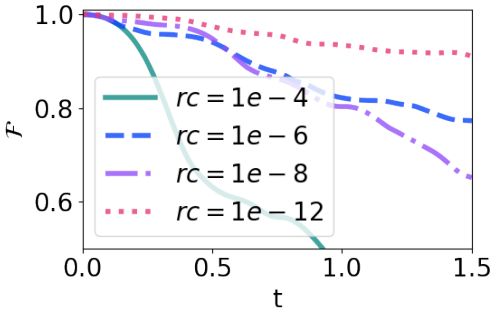

FIG. S8. Fidelity of the variationally time-evolved wavefunction with respect to the exact one as a function of time. Different ratios, rc, for cutting off small singular values are employed. These results are obtained for the case of the free particle with 5 qubits and variational form vf2, depth 3.

Finally, we vary the initial width $\mathcal{B}$ of the wavepacket. Interestingly, we observe that the results are much improved when increasing the initial width (see Fig. S10). The latter influences the overall spread of the wavepacket during the evolution. The difference between initial and final width is 0.841, 0.148 and 0.028 when $\mathcal{B} = 1/\sqrt{2}$, $\mathcal{B} = 2/\sqrt{2}$ and $\mathcal{B} = 3/\sqrt{2}$, respectively. These results suggest that the spread of the wavepacket is difficult to capture with the grid-based VTE.

To validate those observations, we run the VTE of a wavepacket oscillating in a harmonic potential without spread. The space is discretized in 6 qubits as in the simulations of the main text. We also keep the same initial conditions $(x_0, p_0) = (-3.5, 2)$, and the same variational form, vf1 depth 5 in position space. This time, however, the initial width is taken to be $\mathcal{B} = \mathcal{B}_{\rm gs} = 0.6$, where $\mathcal{B}_{\rm gs}$ is the width of Hamiltonian's ground state. Fig. S11 confirms our previous observations: the results in the case of a non-changing width are much improved compared to the results of the main text in which the wavepacket's width changes over time. This leads to the conclusion that the VTE performs reasonably well (with few parameters) for simple dynamics.

We then study the effect of increasing the precision in the grid mesh on the dynamics of the harmonic oscillator. The initial conditions are the ones of the main text: $\mathcal{B} = 1/\sqrt{2}$ and $(x_0, p_0) = (-3.5, 2)$. The space is discretized with 6, 7 and 8 qubits corresponding to 64, 128 and 256 grid points, respectively. The variational form is always taken to be vf1. The results are shown in Fig. S12. We employ both the position and momentum representations of the wavefunction (indicated with x and p in Fig. S12, respectively). The different depths and corresponding number of parameters are also indicated in the legend. The fidelities shown in Fig. S12 are computed from the variationally time evolved wavefunctions with respect to the exactly evolved ones discretized on the same grid. In other words, both the reference and the variational wavefunctions are expressed in the same number of qubits. In all cases, we see that the correct dynamics are recovered in the limit of the number of parameters, n_p, approaching the size of the Hilbert space. In the momentum space, the number of parameters needed to maintain an accuracy of $\mathcal{F} > 95\%$ over the

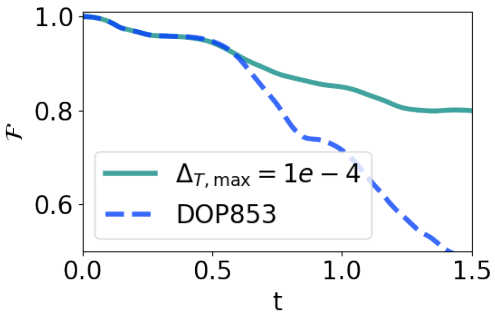

FIG. S9. Fidelity of the variationally time-evolved wavefunction with respect to the exact one as a function of time, obtained with different ordinary differential equation solvers. The full line corresponds to the Runge-Kutta 5(4) solver used throughout this work but with a maximal time step fixed at 10^{-4}. On the other hand, the dashed line was obtained with an explicit Runge-Kutta method of order 8 as implemented in SciPy [2]. These results are obtained for the case of the free particle with 5 qubits and variational form vf2, depth 3.

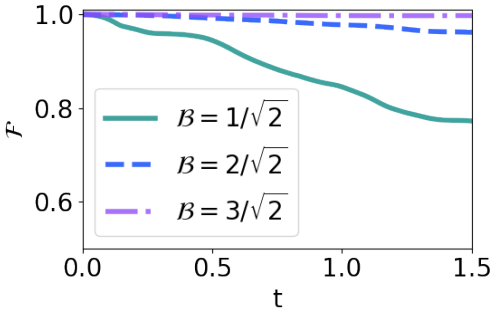

FIG. S10. Fidelity of the variationally time-evolved wavefunction with respect to the exact one as a function of time and for different values of the width, $\mathcal{B}$, of the initial wavepacket. These results are obtained for the case of the free particle with 5 qubits and variational form vf2, depth 3.

whole time range remains low for $N_q = 6$ and $N_q = 7$. It also shows a good scaling behavior when going from 6 to 7 qubits. Indeed, if 60 parameters are necessary in the 6-qubit case, this number only raises to 84 when we double the number of grid points (7 qubits). However, we observe a drop in accuracy when going to 8 qubits. In this case, 416 parameters (for a full Hilbert space represented with 510 real parameters) were not enough to get accurate dynamics both in position and momentum spaces. These results show the influence of the grid mesh on the accuracy of the VTE. The observed non-monotonic behavior pinpoints the strong correlation existing between the different numerical factors, such as N_q and rc. It is important to note that those numerical instabilities are always corrected for when the number of parameters is high enough.

We repeat the simulation of the same harmonic oscillator system for different values of rc, the cutoff ratio of small singular value for the inversion of the matrix M. Those dynamics are obtained with 6, 7, and 8 qubits. The results are shown in Fig. S13. We employ variational form vf1 in position (x) and momentum (p) space, and for different depths (d) as indicated in the legend of Fig. S13. As opposed to the results of Fig. S8, in this case, decreasing the value of rc does not improve the results but even worsens them slightly. On the other hand, we observe improved results when increasing rc with thinner a grid mesh (Fig. S13(c)). This shows again that the numerical effects are correlated and system dependent.

In conclusion, we highlight the following point:

- Heuristic variational forms have the flexibility to accurately and efficiently, i. e., with few variational parameters, describe the targeted wavefunctions at all times of their dynamics. The loss of accuracy observed throughout the different simulations is an inherent effect of the method.

- When the number of variational parameters is insufficient, the dynamics strongly depend on the numerical setup

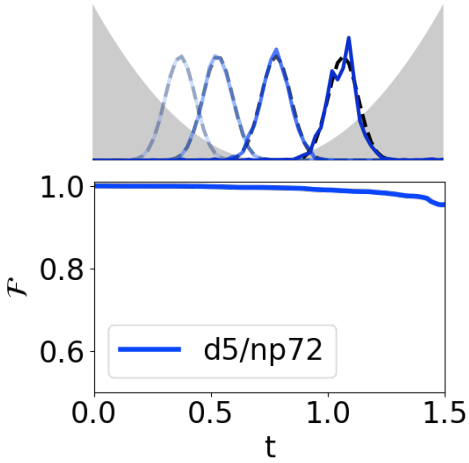

FIG. S11. *Top* Snapshots of the exact (dashed lines) and the variationally time-evolved (full lines) modulus squared wavefunctions at times $t = 0.00, 0.45, 0.91$, and 1.5 of the harmonic oscillator with a non-spreading width $\mathcal{B} = 0.6$.
Bottom Fidelity of the variationally time-evolved wavefunction with respect to the exact one as a function of time. These results are obtained for the case of the harmonic oscillator with width $\mathcal{B} = 0.6$, 6 qubits, and variational form vf1 depth 5 in position space.

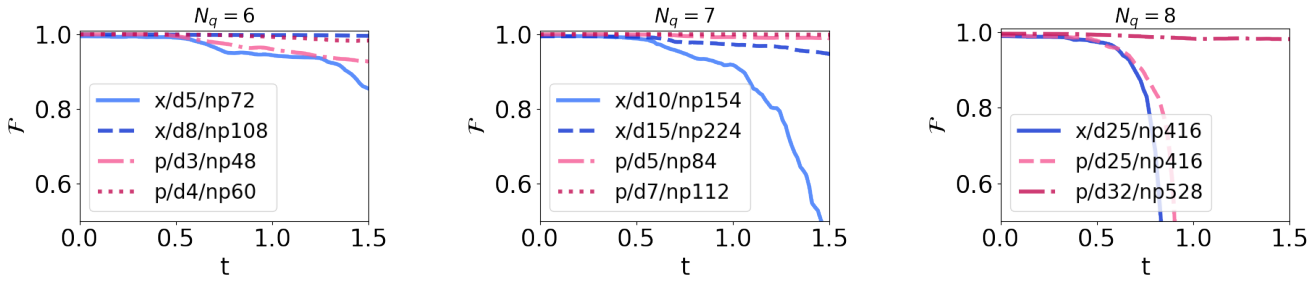

(a) 64 grid points (b) 128 grid points (c) 256 grid points

FIG. S12. Fidelity of the variationally time-evolved wavefunction with respect to the exact one as a function of time. These results are obtained for the case of the harmonic oscillator with variational form vf1. The space is discretized with (a) 6 qubits, (b) 7 qubits, and (c) 8 qubits.

of the simulation (grid mesh size, reconditioning number, initial parameters, etc).

- The correct dynamics are always recovered by increasing the number of variational parameters. In this case, the algorithm is stable.
- The more complex the dynamics is, the larger is the number of needed parameters.
- In all cases presented here, the expression of the wavefunction in momentum space improves the results.

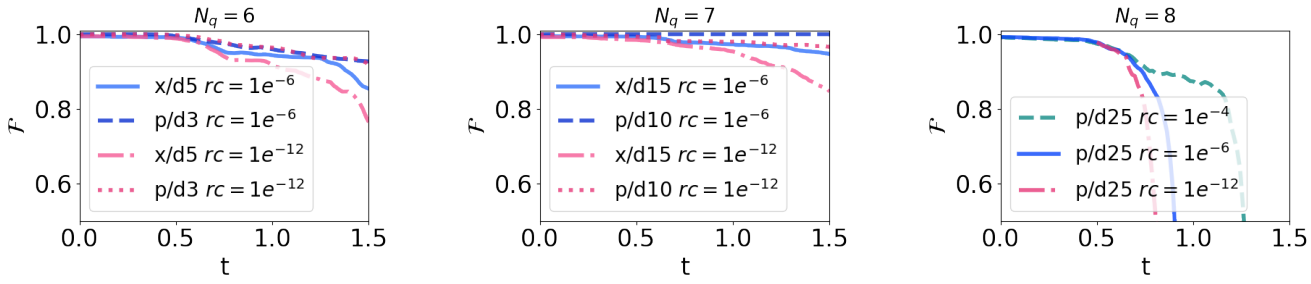

(a) 64 grid points (b) 128 grid points (c) 256 grid points

FIG. S13. Fidelity of the variationally time-evolved wavefunction with respect to the exact one as a function of time. These results are obtained for the case of the harmonic oscillator with variational form vf1, and for different values rc for cutting off small singular values. The space is discretized with (a) 6 qubits, (b) 7 qubits, and (c) 8 qubits.

VI. VARIATIONAL FORMS MIXING POSITION AND MOMENTUM SPACES

In the main text, we discuss the improvement of the results when defining the *Ansatz* in the momentum space, i. e., by adding a QFT at the end of the circuit. Here, we show the results obtained by mixing momentum and position space in the variational form. More explicitly, the *Ansatz* is now composed of several parts; first, a part of given depth in position space, followed by an inverse QFT, then another piece of variational circuit with its own depth, and finally a QFT closing the circuit. We refer to the part enclosed by the QFTs as the momentum part. We vary the depths of the position and momentum parts. The results, shown in Fig. S14, do not highlight any improvement in the performance.

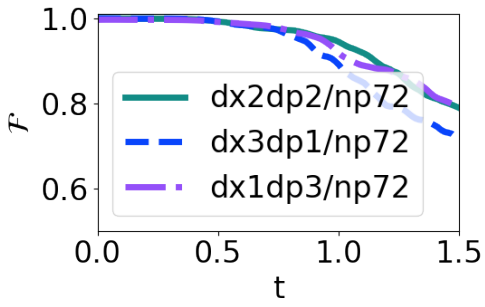

FIG. S14. Fidelity of the variationally time-evolved wavefunction with respect to the exact one as a function of time. These results are obtained for the case of the Eckart barrier with 6 qubits. The quantum circuit corresponds to variational form vf1 with alternating layers in position and momentum space of depths given in the legend.

[1] R. Martinazzo and I. Burghardt, Physical Review Letters **124**, 150601 (2020).
[2] P. Virtanen, R. Gommers, T. E. Oliphant, M. Haberland, T. Reddy, D. Cournapeau, E. Burovski, P. Peterson, W. Weckesser, J. Bright, S. J. van der Walt, M. Brett, J. Wilson, K. J. Millman, N. Mayorov, A. R. J. Nelson, E. Jones, R. Kern, E. Larson, C. J. Carey, İ. Polat, Y. Feng, E. W. Moore, J. VanderPlas, D. Laxalde, J. Perktold, R. Cimrman, I. Henriksen, E. A. Quintero, C. R. Harris, A. M. Archibald, A. H. Ribeiro, F. Pedregosa, P. van Mulbregt, and SciPy 1.0 Contributors, Nature Methods **17**, 261 (2020).